PCCP

ROYAL SOCIETY OF CHEMISTRY

PAPER

View Article Online
View Journal | View Issue



Cite this: *Phys. Chem. Chem. Phys.*, 2020, **22**, 3921

# Prediction of the $Au_4S$ crystal *via* a superatom network model: from clusters to solids†

Qiman Liu,‡[a] Chengyu Zhang,‡[a] Chang Xu,[a] Shuanglin Hu*[b] and Longjiu Cheng *[ac]

Received 15th November 2019,
Accepted 16th January 2020

DOI: 10.1039/c9cp06180k

rsc.li/pccp

Owing to their unique properties, thiolate-protected gold clusters (denoted as $Au_n(SR)_m$) have attracted intense research interest both experimentally and theoretically. The superatom complex (SAC) and superatom network (SAN) models are significantly well-known concepts to explain the electronic stability of $Au_n(SR)_m$. Based on the structural characters of $Au_n(SR)_m$, the tetrahedral $Au_4$ unit was found to be an elementary building block and used to design a series of tetrahedron-network clusters. In this work, we first build a $Au_{22}(\mu_4\text{-S})(SH)_{12}$ cluster consisting of a network of four non-conjugated tetrahedral $Au_4$ units and confirm that it is a local minimum on the potential energy surface by density functional theory calculations. Chemical bonding analysis by the AdNDP method reveals that the electronic structure of $Au_{22}(\mu_4\text{-S})(SH)_{12}$ follows the SAN (4 × 2e) model. Based on the structural character of the $Au_{22}(\mu_4\text{-S})(SH)_{12}$ cluster, we utilize the diamond lattice as a template to construct a stable $Au_4S$ crystal in which each S atom binds to four $Au_4$ superatoms. The computational results demonstrate that the structure has rather good dynamic and thermal stabilities, and it is an indirect semiconductor with a band gap of 2.68 eV at the HSE06 level. Chemical bonding analysis performed by the SSAdNDP method reveals that the $Au_4S$ can be seen as a SAN crystal. These bonding patterns and properties of the solid provide references for further investigation of cluster-assembled materials.



## Introduction

Thiolate-protected gold clusters, denoted as $Au_n(SR)_m$, have attracted widespread research interest due to their extraordinary stability, physicochemical properties, and many promising applications in the field of catalysis, chemical sensing, biolabeling, and so on.[1–15]

In recent years, marked advances were made in determining the structures of $Au_m(SR)_n$ clusters from both experiments and theory. Particularly, after two breakthroughs of crystallization of $Au_{25}(SR)_{18}^{-}$[7,11] and $Au_{102}(SR)_{44}$[3] clusters, a number of $Au_m(SR)_n$ clusters with different compositions were successfully resolved *via* X-ray crystallography, *e.g.*, $Au_{18}(SR)_{14}$,[16,17] $Au_{20}(SR)_{16}$,[18] $Au_{23}(SR)_{16}^{-}$,[19] $Au_{28}(SR)_{20}$,[20] $Au_{30}S(SR)_{18}$,[21] $Au_{36}(SR)_{24}$,[22] $Au_{38}(SR)_{24}$,[23] $Au_{68}(SR)_{34}$,[24] and $Au_{130}(SR)_{50}$.[25] Based on these structures, the growth mechanism of gold clusters with sizes is explored and two evolution paths are summarized (Fig. 1), including core growth and staple motif growth. In a typical core growth process, the $Au_m(SR)_n$ cluster can be subdivided into a compact Au core and a set of organothiolate ligands. The Au core often exhibits a highly symmetrical geometry with a closed-shell singlet ground state. To explain the high stability of certain magic number $Au_m(SR)_n$ clusters, Häkkinen *et al.* proposed the superatom complex (SAC) concept based on the jellium model.[26] According to the SAC model, $Au_{102}(SR)_{44}$ and $Au_{25}(SR)_{18}^{-}$ have 58 and 8

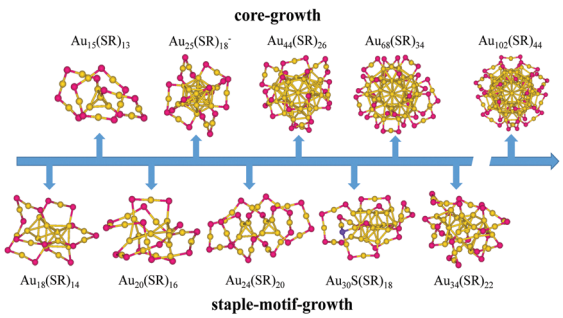


Fig. 1 Structural evolution routes of thiolate-protected gold clusters that have been resolved by either experiments or predicted by theory.

[a] *Department of Chemistry, Anhui University, Hefei, Anhui 230601, P. R. China. E-mail: clj@ustc.edu*
[b] *Institute of Nuclear Physics and Chemistry, China Academy of Engineering Physics, Mianyang 621900, Sichuan, China. E-mail: hushuanglin@caep.cn*
[c] *Anhui Province Key Laboratory of Chemistry for Inorganic/Organic Hybrid Functionalized Materials, Hefei, Anhui, 230601, P. R. China*

† Electronic supplementary information (ESI) available: The AdNDP localized natural bonding orbitals of the valence shells of the $Au_{22}(\mu_4\text{-S})(SH)_{12}$ cluster. The SSAdNDP chemical bonding pattern and the electronic band structure of the $Au_4S$ crystal. See DOI: 10.1039/c9cp06180k

‡ These two authors contributed equally to this work.

valence electrons contributed from the metallic Au-core, respectively, which are indeed magic numbers corresponding to the closed electronic shells in the framework of the jellium model.

However, the clusters in staple motif growth cannot all be understood in the framework of the SAC model. To understand the electronic stability of the nonspherical structures of metal clusters, Cheng *et al.* developed the superatom-network (SAN) model.[27] It was found that, experimentally synthesized $Au_{18}(SR)_{14}$,[16,17] $Au_{20}(SR)_{16}$,[18] and $Au_{24}(SR)_{20}$[28] are 4 valence-electron (4e) compounds following the SAN model. The structure of the $Au_{18}(SR)_{14}$ cluster features a bi-octahedral $Au_9$ core protected by three kinds of staple motifs including three monomers, a dimer and a tetramer. According to the SAN model, the $Au_9$ core of the cluster can be considered as a unique integration of two fused octahedral $Au_6$ superatoms by sharing one triangular face. The structure of $Au_{20}(SR)_{16}$ has a vertex-sharing bi-tetrahedral $Au_7$ kernel protected by monomeric and trimeric staple motifs as well as a giant octameric $Au_8(SR)_8$ ring. The structure of $Au_{24}(SR)_{20}$ has a bi-tetrahedral $Au_8$ kernel with four tetrameric staple motifs. The electronic stabilities of these two clusters follow the SAN model, and both of their Au kernels can be seen as networks of two $Au_4$ superatoms. The $Au_{22}(SR)_{18}$ cluster possesses the same $Au_7$ kernel with the $Au_{20}(SR)_{16}$, which can also be viewed as a union of two 4c–2e tetrahedron $Au_4$ superatoms. Moreover, $Au_{44}(SR)_{28}$,[29] $Au_{52}(SR)_{32}$,[30] $Au_{60}(SR)_{36}$,[31] and $Au_{76}(SR)_{44}$[32] clusters exhibit unique double-helix structures that consist of networks of tetrahedral $Au_4$ superatoms. Recently, Pei *et al.* reported that the Au cores of face-centered-cubic (fcc-type) $Au_m(SR)_n$ clusters have a tetrahedral $Au_4$ growth pattern and predicted a series of tetrahedron networks of fcc-type $Au_m(SR)_n$ clusters.[29,33–35]

The ''divide-and-protect'' model was developed by Häkkinen *et al.*,[36] that is, the $Au_m(SR)_n$ cluster can be seen as an Au kernel protected by various forms of staple motifs. To date, different kinds of staple motifs in $Au_m(SR)_n$ clusters have been discovered or proposed. Among them, most cases are two-coordinate $\mu_2$-S staple motifs, for example, the monomeric (–SR–Au–SR–), dimeric (–SR–Au–SR–Au–SR–) and trimeric (–SR–Au–SR–Au–SR–Au–SR–), as well as pentameric (–SR–Au–SR–Au–SR–Au–SR–Au–SR–Au–SR–) staple motifs. Furthermore, large thiolate rings such as $Au_6(SR)_6$ and $Au_8(SR)_8$ rings were found in $Au_{22}(SR)_{18}$ and $Au_{20}(SR)_{16}$ clusters, respectively. In 2013, Dass and Zheng crystallized the $Au_{30}S(SR)_{18}$ cluster,[21,37] and reported a novel $\mu_3$-S bridging in $Au_m(SR)_n$ clusters. In fact, the $\mu_3$-S surface motif had been observed in the $Au_3Ag(\mu_3\text{-}S)(PPh_2py)_3^{2+}$ cluster earlier.[38] Later, experimentally determined $Au_n(SR)_m$ clusters with one or two $\mu_3$-S bridges included $Au_{21}S(SR)_{15}$, $Au_{38}S_2(SR)_{20}$ and $Au_{103}S_2(SR)_{41}$. Notably, the $\mu_4$-S staple motif has been found in $Au_{60}S_6(SCH_2Ph)_{36}$[39] and $Au_{60}S_7(SCH_2Ph)_{36}$[40] clusters.

The tetrahedral $Au_4$ unit is a popular structural pattern and is regarded as an elementary block among the $Au_n(SR)_m$ clusters, which has been used to design a series of tetrahedron-network clusters.[34,41–43] According to the SAN model, we build a $Au_{22}(\mu_4\text{-}S)(SH)_{12}$ cluster consisting of a network of four tetrahedral $Au_4$ units and confirm that the cluster is a local minimum on the potential energy surface by means of density functional theory (DFT) computations. Based on the structural character of the $Au_{22}(\mu_4\text{-}S)(SH)_{12}$ cluster, we utilize a diamond lattice as a template to construct a stable $Au_4S$ crystal in which each S atom binds to four $Au_4$ superatoms. Our DFT computations demonstrate that the $Au_4S$ has rather good thermal and kinetic stabilities, and it is an indirect semiconductor with a large band gap, thus promising for application in optoelectronics and electronics. Such cluster-assembled materials on the basis of cluster superatoms can be viewed as expansions of SAN complexes.

## Computational methods and details

### DFT computations

For the $Au_{22}(\mu_4\text{-}S)(SH)_{12}$ cluster, geometry optimization, frequency analysis and subsequent calculations were performed at the PBE level[44] of theory with the def2-TZVP basis set[45] as implemented in the Gaussian 09 package.[46] The basis set, which is used in connection with the relativistic effective core potentials for the Au atom and all electrons for S and H atoms, has been proven reliable in the prediction of $Au_m(SR)_n$ clusters.[34,47] For the $Au_4S$ solid, DFT computations were carried out by using the projector-augmented-wave (PAW) method in the Vienna *ab initio* simulation package (VASP).[48] The PBE density functional[44] and a kinetic energy cutoff of 450 eV for the plane-wave basis set were used. The Brillouin zones were sampled using $13 \times 13 \times 13$ Monkhorst–Pack *k*-point meshes. The calculations of the phonon spectra were done using the PHONOPY program.[49] The chemical bonding analysis of $Au_4S$ was performed using the Solid State Adaptive Natural Density Partitioning (SSAdNDP) method,[50] which can well clarify the chemical bonding in the aspects of classical lone pairs, two-centre bonds, and multi-centre bonds in clusters, bulk solids and surfaces, and so on. Within the SSAdNDP, the plane-wave density was projected[51] into the def2-SVP[52] basis set. The visualization of the SSAdNDP results was realized using the VESTA software.[53]

### Molecular dynamics simulations

*Ab initio* molecular dynamics (AIMD) simulations were performed to examine the thermal stability of the $Au_4S$ structure. To be accurate and reliable, the initial configuration of $Au_4S$ involving $3 \times 2$ unit cells was used at several temperatures. Each AIMD simulation (*NVT* ensemble) lasted for 10 ps with a time step of 1.0 fs. The temperatures were controlled using the Nosé–Hoover method.[54]

## Results and discussion

### Geometric and electronic characters of the $Au_{22}(\mu_4\text{-}S)(SH)_{12}$ cluster

As we know, the tetrahedral $Au_4$ unit as an elementary building block has been successfully used to design a series of $Au_n(SR)_m$ clusters.[34,42] Here, according to the SAN model, we build a

 

$Au_{22}(\mu_4\text{-S})(SH)_{12}$ cluster which is composed of four tetrahedral $Au_4$ units, six monomeric staple motifs and a $\mu_4$-S. It is worth noting that the $\mu_4$-S binds to four $Au_4$ units. To segregate $Au_4$ units, the $\mu_4$-S motif is a requisite in the cluster. The optimized $Au_{22}(\mu_4\text{-S})(SH)_{12}$ cluster with a fairly large HOMO–LUMO gap ($E_{HL}$) of 2.69 eV is displayed in Fig. 2a, and it is verified to be a true local minimum on the potential energy surface by frequency check. The large gap indicates high electronic stability. The bond lengths of ($\mu_4$-S)-Au are 2.35 Å, and the Au–Au bond lengths within the $Au_4$ tetrahedra are in the range of 2.74–2.76 Å, which are very close to previous experimental and theoretical results.[29,55–57] The distance between different bridging Au atoms (3.78 Å) is very close to the van der Waals distance (3.80 Å) because $Au_4$ units are segregated by the $\mu_4$-S atom. So it is not possible that four bridging Au atoms form another intact tetrahedron. To verify that the $Au_{22}(\mu_4\text{-S})(SH)_{12}$ cluster consists of a network of four non-conjugated tetrahedral $Au_4$ superatoms, chemical bonding analysis is carried out by the adaptive natural density partitioning (AdNDP) method.[58,59] The AdNDP result in Fig. 2b indicates that there are four 4c–2e (four-center two-electron) $\sigma$ bonds with occupancy numbers (ON) = 1.79 $|e|$. The details for the AdNDP chemical bonding analysis are shown in Fig. S1 of the ESI.† Thus the electronic structure of the cluster follows the SAN (4 × 2e) model.

The calculated nucleus-independent chemical shift (NICS) value is now a popular measurement for the aromaticity or shell closure of delocalized bonding.[60] Here we employ a NICS-scan method[61] to further clarify the existence of $Au_4$ superatoms in the $Au_{22}(\mu_4\text{-S})(SH)_{12}$, which was successfully used to verify the SAN model in the previous $Au_{70}S_{20}(PPh_3)_{12}$, $Au_{28}(SR)_{20}$, $Au_{30}S_2(SR)_{18}$ and $Au_{20}(SR)_{16}$ clusters.[27,56,62] Fig. 2c displays the NICS–scan curve of the $Au_{22}(\mu_4\text{-S})(SH)_{12}$ cluster along the centers of two $Au_4$ superatoms within the range of −5.0–5.0 Å. The positions of NICS(0) are located at the geometric centers of these two $Au_4$ superatoms. Considering the symmetry of the cluster, we only show one scan curve of the $Au_{22}(\mu_4\text{-S})(SH)_{12}$. The NICS(0) values of the $Au_4$ superatoms are both −34.3 ppm, much smaller than that of the famous aromatic benzene (−9.7 ppm).[63] Moreover, there are two dotted ovals in the figure, indicating the presence of two non-conjugate $Au_4$ superatoms, which give extra support for the SAN model from the aromatic view.

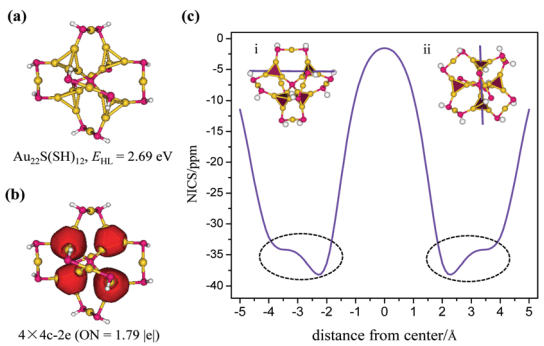


Fig. 2 (a) Optimized geometric structure of the $Au_{22}(\mu_4\text{-S})(SH)_{12}$ cluster. H, white; Au, yellow and S, red. (b) AdNDP localized natural bonding orbitals of the $Au_{22}(\mu_4\text{-S})(SH)_{12}$ cluster. (c) NICScc-scan curve of the $Au_{22}(\mu_4\text{-S})(SH)_{12}$ cluster, which is the scan along the centers of the two $Au_4$ superatoms in the range of −5.0–5.0 Å. The dotted ovals in the figure signal show the presence of $Au_4$ superatoms. The structures labelled in (i) and (ii) indicate two views of the scan.

## Geometric structure, stability, and electronic character of the $Au_4S$ crystal

Earlier Burdett and Lee were aware that a tetrahedral carbon atom in the diamond lattice can be substituted with a $C_4$ tetrahedron to form a new super-tetrahedral structure of carbon.[64] Similarly, super-tetrahedral boron structures can be obtained by the replacement of carbon atoms in the diamond lattice with tetrahedral $B_4$ fragments.[65,66] Inspired by the bonding pattern of the $Au_{22}(\mu_4\text{-S})(SH)_{12}$ cluster, we also use the diamond lattice as a template where all carbon atoms are substituted by $Au_4$ units and S atoms to design a diamond-like $Au_4S$ solid. The optimized structure of our designed $Au_4S$ crystal is shown in Fig. 3a. One unit cell of $Au_4S$ is composed of 16 Au and 4 S atoms, with the optimized lattice constants being $a = b = c$ = 9.21 Å. Similar to the $Au_{22}(\mu_4\text{-S})(SH)_{12}$ cluster, in the $Au_4S$ crystal each S atom binds to four $Au_4$ units, and the Au–Au and Au–S bond lengths are 2.73 and 2.32 Å, respectively. In comparison, the Au–S bond length of the experimentally known $P_n3_m$ $Au_2S$ structure is 2.18 Å.[67,68]

For Au ($5d^{10}6s^1$) of the $Au_4S$, the $5d^{10}$ electrons as lone pairs (LPs) are localized and $6s^1$ are free valence electrons. According to the electron counting rule, the $Au_4$ unit has four valence electrons, so each Au atom of the $Au_4S$ should transfer 0.5 valence electrons to the $\mu_4$-S to offset its 2e valence electrons. Thus the whole $Au_4$ unit retains 2e valence electrons in total, denoted as the $Au_4$ superatom. To gain a deep insight into the chemical bonding in the $Au_4S$, we used an extension of the periodic natural bond orbital method, namely the Solid State Adaptive Natural Density Partitioning (SSAdNDP) method. SSAdNDP analysis is used to identify both localized ($nc$−2e bonds, $n \leq 2$) as well as delocalized ($nc$−2e bonds, $n > 2$) bonding elements in the $Au_4S$. In total, there are 200 valence electrons per unit cell. The SSAdNDP analysis identifies that there are five d-type LPs on each Au atom with ON = (1.93–1.99)

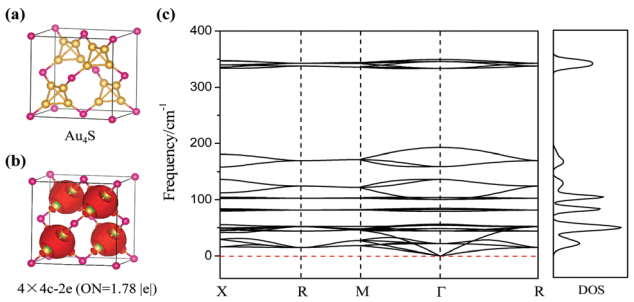


Fig. 3 (a) Optimized structure of the $Au_4S$ crystal with the unit cell. The yellow and red spheres represent the Au and S atoms, respectively. (b) Schematic of the SSAdNDP chemical bonding pattern of the $Au_4S$. (c) Calculated phonon dispersion curves along the high-symmetry lines in the first Brillouin zone and phonon density of states (DOS) for the $Au_4S$.

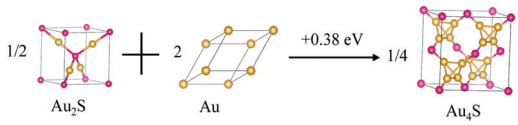


Fig. 4 Formation of $Au_4S$ from experimentally available $Au_2S$ and Au solids. Reaction enthalpy (eV) is labeled.

$|e|$, thus hinting at their no participation in the bond formation. Moreover, there are sixteen 2c–2e Au–S σ bonds with ON = 1.92 $|e|$ as well as four 4c−2e σ bonds with ON = 1.78 $|e|$. These four 4c–2e σ bonds are shown in Fig. 3b. The details of the SSAdNDP chemical bonding analysis are shown in Fig. S2 (ESI†). Thus the $Au_4S$ can be seen as a SAN crystal.

To test the dynamic stability of the $Au_4S$ structure, phonon calculations are performed along the high-symmetry lines in the first Brillouin zone. As shown in Fig. 3c, all the frequencies are real and no imaginary phonon frequencies exist in the whole Brillouin zone, indicating that the $Au_4S$ is kinetically stable. It is noteworthy that the highest frequency can reach up to 349 $cm^{-1}$, suggesting the robustness of the Au–S interaction.[69]

For any newly predicted materials, thermal stability is a crucial point for experimental synthesis. Here we take the experimentally available $Au_2S$ and fcc-Au primitive cells as references to evaluate the experimental feasibility of $Au_4S$. The enthalpy of formation of $Au_4S$ is calculated and the result is shown in Fig. 4. This process is the endothermal reaction with a reaction energy ($E_{re}$) of +0.38 eV, indicating that the $Au_2S$ is energetically more preferable. But the small $E_{re}$ value indicates that the $Au_4S$ is also an energetically optimal candidate. Thus we believe that it is realizable to synthesize $Au_4S$ by the same or a similar method used for synthesizing $Au_2S$.

We further performed AIMD simulations to evaluate the thermal stability of the $Au_4S$ structure. A supercell containing 3 × 2 unit cells (96 Au atoms and 24 S atoms) was adopted as the initial configuration. The simulations lasted for 10 ps with a time step of 1.0 fs at initial temperatures of 300, 500, and 700 K, respectively. Furthermore, snapshots were extracted every 20 fs for demonstration. Energy fluctuation depending on simulated time at the selected temperature and the snapshot of $Au_4S$ after a 10 ps AIMD simulation are plotted in Fig. 5. It can be observed that the structure of $Au_4S$ maintains integrity during the 10 ps

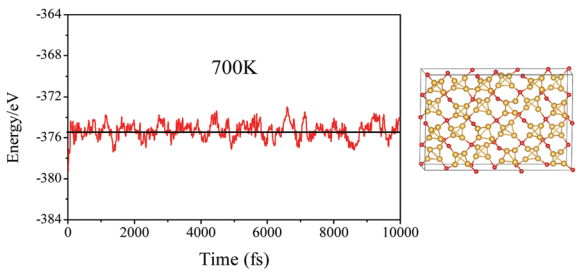


Fig. 5 Energy fluctuation depending on simulated time in molecular dynamics simulation at 700 K and the snapshot of the $Au_4S$ after a 10 ps MD simulation.

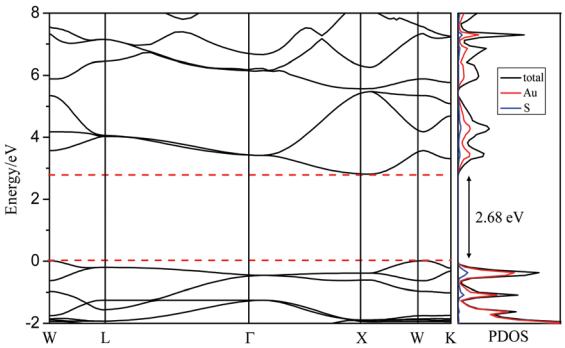


Fig. 6 Electronic band structure and projected density of states of the $Au_4S$ at the HSE06 level. The Fermi level is set at zero.

AIMD simulation at a temperature of 700 K, suggesting its good thermal stability in the high temperature environment.

Based on the structural stability, we next investigated the potential electronic properties of the $Au_4S$. The energy band structures and projected density of states (PDOS) were computed at the PBE and HSE06 levels of theory, respectively. Fig. 6 shows the electronic band structure and PDOS of the $Au_4S$ calculated at the HSE06 level of theory. It is clear that the $Au_4S$ is an indirect-bandgap semiconductor because the valence band maximum is located on the *W* point and the conduction band minimum is at the *X* point. The band gap of $Au_4S$ is 1.84 eV at the PBE level (Fig. S3, ESI†), and is 2.68 eV at the more accurate HSE06 functional. It is reasonable to assume that the value of the band gap at the HSE06 level is closer to the realistic band gap, thus promising for applications in optoelectronics and electronics.[69] Moreover, analysis of the PDOS reveals that the energy states near the Fermi level mainly come from the orbitals of Au atoms.

In order to expand SAN crystals, the same construction principle was used in the design of $Ag_4S$ and $Cu_4O$. After relaxation, these two solids have similar geometric and electronic characters to the $Au_4S$, as shown in Fig. S4 and S5 (ESI†).

## Conclusions

In summary, according to the SAN model, we built the $Au_{22}(\mu_4\text{-}S)(SH)_{12}$ cluster which is composed of four tetrahedral $Au_4$ units, six monomeric staple motifs and a $\mu_4$-S. Using systematic density functional theory calculations, the cluster is confirmed to be a local minimum on the potential energy surface and has a large HOMO–LUMO energy gap of 2.69 eV. AdNDP and NICS-scan analyses reveal that the electronic structure of the $Au_{22}(\mu_4\text{-}S)(SH)_{12}$ follows the SAN (4 × 2e) model. Based on the structural characters of the $Au_{22}(\mu_4\text{-}S)(SH)_{12}$ cluster, we use the diamond lattice as a template to design a novel super-tetrahedral $Au_4S$ solid, where each S atom binds to four $Au_4$ units. The computational results demonstrate that the $Au_4S$ structure has rather good dynamic and thermal stabilities, and it is a semiconductor with an indirect band gap of 2.68 eV at the HSE06 level. Chemical bonding analysis given by SSAdNDP reveals that the $Au_4S$ can be seen as a SAN crystal.

Moreover, SAN crystals $Ag_4S$ and $Cu_4O$ are also designed, which have similar geometric and electronic characters to the $Au_4S$.

Our studies reveal that cluster-assembled materials based on $Au_4$ superatoms and sulfur atoms can be viewed as expansions of SAN complexes. We hope the studies attract more attention on investigating superatomic materials with novel chemical bonding and properties.

## Conflicts of interest

There are no conflicts to declare.

## Acknowledgements

This work was financed by the National Natural Science Foundation of China (21873001), by the National Key Research and Development Program of China (2016YFB0201203), by the President foundation of China Academy of Engineering Physics (YZJJLX2016004), and by the Foundation of Distinguished Young Scientists of Anhui Province. The calculations were carried out at the High-Performance Computing Center of Anhui University, the National Super-Computing Center at Wuxi, and the Shanghai super computer center.

## Notes and references

1 R. Jin, C. Zeng, M. Zhou and Y. Chen, *Chem. Rev.*, 2016, **116**, 10346–10413.
2 H. Häkkinen, *Nat. Chem.*, 2012, **4**, 443.
3 P. D. Jadzinsky, G. Calero, C. J. Ackerson, D. A. Bushnell and R. D. Kornberg, *Science*, 2007, **318**, 430–433.
4 I. Dolamic, B. Varnholt and T. Bürgi, *Nat. Commun.*, 2015, **6**, 7117.
5 M. Zhu, H. Qian, X. Meng, S. Jin, Z. Wu and R. Jin, *Nano Lett.*, 2011, **11**, 3963–3969.
6 N. L. Rosi, D. A. Giljohann, C. S. Thaxton, A. K. R. Lytton-Jean, M. S. Han and C. A. Mirkin, *Science*, 2006, **312**, 1027–1030.
7 M. W. Heaven, A. Dass, P. S. White, K. M. Holt and R. W. Murray, *J. Am. Chem. Soc.*, 2008, **130**, 3754–3755.
8 S. Chen, L. Xiong, S. Wang, Z. Ma, S. Jin, H. Sheng, Y. Pei and M. Zhu, *J. Am. Chem. Soc.*, 2016, **138**, 10754–10757.
9 J. F. Parker, C. A. Fields-Zinna and R. W. Murray, *Acc. Chem. Res.*, 2010, **43**, 1289–1296.
10 C. Liu, S. Lin, Y. Pei and X. C. Zeng, *J. Am. Chem. Soc.*, 2013, **135**, 18067–18079.
11 M. Zhu, C. M. Aikens, F. J. Hollander, G. C. Schatz and R. Jin, *J. Am. Chem. Soc.*, 2008, **130**, 5883–5885.
12 D.-e. Jiang, S. H. Overbury and S. Dai, *J. Am. Chem. Soc.*, 2013, **135**, 8786–8789.
13 O. Lopez-Acevedo, K. A. Kacprzak, J. Akola and H. Häkkinen, *Nat. Chem.*, 2010, **2**, 329.
14 H. Tsunoyama, H. Sakurai, Y. Negishi and T. Tsukuda, *J. Am. Chem. Soc.*, 2005, **127**, 9374–9375.
15 S. Knoppe, I. Dolamic, A. Dass and T. Bürgi, *Angew. Chem., Int. Ed.*, 2012, **51**, 7589–7591.
16 S. Chen, S. Wang, J. Zhong, Y. Song, J. Zhang, H. Sheng, Y. Pei and M. Zhu, *Angew. Chem., Int. Ed.*, 2015, **54**, 3145–3149.
17 A. Das, C. Liu, H. Y. Byun, K. Nobusada, S. Zhao, N. Rosi and R. Jin, *Angew. Chem., Int. Ed.*, 2015, **54**, 3140–3144.
18 C. Zeng, C. Liu, Y. Chen, N. L. Rosi and R. Jin, *J. Am. Chem. Soc.*, 2014, **136**, 11922–11925.
19 A. Das, T. Li, K. Nobusada, C. Zeng, N. L. Rosi and R. Jin, *J. Am. Chem. Soc.*, 2013, **135**, 18264–18267.
20 C. Zeng, T. Li, A. Das, N. L. Rosi and R. Jin, *J. Am. Chem. Soc.*, 2013, **135**, 10011–10013.
21 D. Crasto, S. Malola, G. Brosofsky, A. Dass and H. Häkkinen, *J. Am. Chem. Soc.*, 2014, **136**, 5000–5005.
22 C. Zeng, H. Qian, T. Li, G. Li, N. L. Rosi, B. Yoon, R. N. Barnett, R. L. Whetten, U. Landman and R. Jin, *Angew. Chem., Int. Ed.*, 2012, **51**, 13114–13118.
23 H. Qian, W. T. Eckenhoff, Y. Zhu, T. Pintauer and R. Jin, *J. Am. Chem. Soc.*, 2010, **132**, 8280–8281.
24 A. Dass, *J. Am. Chem. Soc.*, 2009, **131**, 11666–11667.
25 Y. Chen, C. Zeng, C. Liu, K. Kirschbaum, C. Gayathri, R. R. Gil, N. L. Rosi and R. Jin, *J. Am. Chem. Soc.*, 2015, **137**, 10076–10079.
26 M. Walter, J. Akola, O. Lopez-Acevedo, P. D. Jadzinsky, G. Calero, C. J. Ackerson, R. L. Whetten, H. Grönbeck and H. Häkkinen, *Proc. Natl. Acad. Sci. U. S. A.*, 2008, **105**, 9157–9162.
27 L. Cheng, Y. Yuan, X. Zhang and J. Yang, *Angew. Chem., Int. Ed.*, 2013, **52**, 9035–9039.
28 A. Das, T. Li, G. Li, K. Nobusada, C. Zeng, N. L. Rosi and R. Jin, *Nanoscale*, 2014, **6**, 6458–6462.
29 Y. Pei, S. Lin, J. Su and C. Liu, *J. Am. Chem. Soc.*, 2013, **135**, 19060–19063.
30 C. Zeng, Y. Chen, C. Liu, K. Nobusada, N. L. Rosi and R. Jin, *Sci. Adv.*, 2015, **1**, 1500425.
31 W. W. Xu, Y. Li, Y. Gao and X. C. Zeng, *Nanoscale*, 2016, **8**, 7396–7401.
32 Z. Ma, P. Wang, G. Zhou, J. Tang, H. Li and Y. Pei, *J. Phys. Chem. C*, 2016, **120**, 13739–13748.
33 L. Xiong, S. Yang, X. Sun, J. Chai, B. Rao, L. Yi, M. Zhu and Y. Pei, *J. Phys. Chem. C*, 2018, **122**, 14898–14907.
34 Y. Pei, P. Wang, Z. Ma and L. Xiong, *Acc. Chem. Res.*, 2019, **52**, 23–33.
35 L. Xiong, B. Peng, Z. Ma, P. Wang and Y. Pei, *Nanoscale*, 2017, **9**, 2895–2902.
36 H. Häkkinen, M. Walter and H. Grönbeck, *J. Phys. Chem. B*, 2006, **110**, 9927–9931.
37 H. Yang, Y. Wang, A. J. Edwards, J. Yan and N. Zheng, *Chem. Commun.*, 2014, **50**, 14325–14327.
38 Q.-M. Wang, Y.-A. Lee, O. Crespo, J. Deaton, C. Tang, H. J. Gysling, M. Concepción Gimeno, C. Larraz, M. D. Villacampa, A. Laguna and R. Eisenberg, *J. Am. Chem. Soc.*, 2004, **126**, 9488–9489.
39 Z. Gan, J. Chen, J. Wang, C. Wang, M.-B. Li, C. Yao, S. Zhuang, A. Xu, L. Li and Z. Wu, *Nat. Commun.*, 2017, **8**, 14739.

40 Z. Gan, J. Chen, L. Liao, H. Zhang and Z. Wu, *J. Phys. Chem. Lett.*, 2018, **9**, 204–208.
41 W. W. Xu, X. C. Zeng and Y. Gao, *Acc. Chem. Res.*, 2018, **51**, 2739–2747.
42 A. Tlahuice-Flores, *J. Phys. Chem. C*, 2019, **123**, 10831–10841.
43 Z. Tian and L. Cheng, *J. Phys. Chem. C*, 2017, **121**, 20458–20467.
44 J. P. Perdew, K. Burke and M. Ernzerhof, *Phys. Rev. Lett.*, 1996, **77**, 3865–3868.
45 F. Weigend and R. Ahlrichs, *Phys. Chem. Chem. Phys.*, 2005, **7**, 3297–3305.
46 M. J. Frisch, *et al.*, *Gaussian 09, Revision B.01*, Gaussian, Inc., Wallingford, CT, 2009.
47 Q. Yao, X. Yuan, V. Fung, Y. Yu, D. T. Leong, D.-e. Jiang and J. Xie, *Nat. Commun.*, 2017, **8**, 927.
48 G. H. Kresse and J. Hafner, *Phys. Rev. B: Condens. Matter Mater. Phys.*, 1993, **47**, 558.
49 A. Togo and I. Tanaka, *Scr. Mater.*, 2015, **108**, 1–5.
50 T. R. Galeev, B. D. Dunnington, J. R. Schmidt and A. I. Boldyrev, *Phys. Chem. Chem. Phys.*, 2013, **15**, 5022–5029.
51 B. D. Dunnington and J. R. Schmidt, *J. Chem. Theory Comput.*, 2012, **8**, 1902–1911.
52 F. Weigend, *Phys. Chem. Chem. Phys.*, 2006, **8**, 1057–1065.
53 K. Momma and F. Izumi, *J. Appl. Crystallogr.*, 2011, **44**, 1272–1276.
54 G. J. Martyna, M. L. Klein and M. Tuckerman, *J. Chem. Phys.*, 1992, **97**, 2635–2643.
55 Z. Tian and L. Cheng, *Nanoscale*, 2016, **8**, 826–834.
56 Z. Tian and L. Cheng, *Phys. Chem. Chem. Phys.*, 2015, **17**, 13421–13428.
57 W. Liu and L. Cheng, *J. Phys. Chem. C*, 2016, **120**, 2432–2438.
58 D. Y. Zubarev and A. I. Boldyrev, *Phys. Chem. Chem. Phys.*, 2008, **10**, 5207–5217.
59 D. Y. Zubarev and A. I. Boldyrev, *J. Org. Chem.*, 2008, **73**, 9251–9258.
60 P. v. R. Schleyer, C. Maerker, A. Dransfeld, H. Jiao and N. J. R. van Eikema Hommes, *J. Am. Chem. Soc.*, 1996, **118**, 6317–6318.
61 A. Stanger, *J. Org. Chem.*, 2006, **71**, 883–893.
62 Z. Tian, Y. Xu and L. Cheng, *Nanomaterials*, 2019, **9**, 1132.
63 P. v. R. Schleyer, M. Manoharan, Z.-X. Wang, B. Kiran, H. Jiao, R. Puchta and N. J. R. van Eikema Hommes, *Org. Lett.*, 2001, **3**, 2465–2468.
64 J. K. Burdett and S. Lee, *J. Am. Chem. Soc.*, 1985, **107**, 3063–3082.
65 I. V. Getmanskii, R. M. Minyaev, D. V. Steglenko, V. V. Koval, S. A. Zaitsev and V. I. Minkin, *Angew. Chem., Int. Ed.*, 2017, **56**, 10118–10122.
66 I. V. Getmanskii, V. V. Koval, A. I. Boldyrev, R. M. Minyaev and V. I. Minkin, *J. Phys. Chem. A*, 2019, **123**, 267–271.
67 K. Ishikawa, T. Isonaga, S. Wakita and Y. Suzuki, *Solid State Ionics*, 1995, **79**, 60–66.
68 D. Santamaría-Pérez, D. Daisenberger, J. Ruiz-Fuertes, T. Marqueño, R. Chulia-Jordan, C. Muehle, M. Jansen, P. Rodriguez-Hernandez, A. Muñoz, E. R. Johnson and A. Otero-de-la-Roza, *Chem. Sci.*, 2019, **10**, 6467–6475.
69 Q. Wu, W. W. Xu, B. Qu, L. Ma, X. Niu, J. Wang and X. C. Zeng, *Mater. Horiz.*, 2017, **4**, 1085–1091.